

ARTICLE OPEN



Inverse design of truss lattice materials with superior buckling resistance

Marco Maurizi , Chao Gao¹ and Filippo Berto¹

Manipulating the architecture of materials to achieve optimal combinations of properties (inverse design) has always been the dream of materials scientists and engineers. Lattices represent an efficient way to obtain lightweight yet strong materials, providing a high degree of tailorability. Despite massive research has been done on lattice architectures, the inverse design problem of complex phenomena (such as structural instability) has remained elusive. Via deep neural network and genetic algorithm, we provide a machine-learning-based approach to inverse-design non-uniformly assembled lattices. Combining basic building blocks, our approach allows us to independently control the geometry and topology of periodic and aperiodic structures. As an example, we inverse-design lattice architectures with superior buckling performance, outperforming traditional reinforced grid-like and bio-inspired lattices by ~30–90% and 10–30%, respectively. Our results provide insights into the buckling behavior of beam-based lattices, opening an avenue for possible applications in modern structures and infrastructures.

npj Computational Materials (2022)8:247; <https://doi.org/10.1038/s41524-022-00938-w>

INTRODUCTION

Architecting the structure of materials as a lattice (i.e., arrangement of solids and voids) from the micro- to the macro-scale has been proven to be an efficient way to obtain lightweight yet strong and stable structural materials^{1–13}. Wood, bone, and glass sponge skeleton are paradigmatic examples of the nature of mechanical efficiency obtained by a variety of geometrical (i.e., shape and relative size of the constituents) and topologically (i.e., how and which constituents are connected) diverse lattices^{14–17}. In the attempt to engineer robust lattices, periodicity (i.e., tessellation of a unit cell in the space) has been harnessed to gain stiffness and strength over stochastic arrangement (e.g., random foams) at the same relative density (i.e., a fraction of material in a bulk volume)¹⁸, leveraging the more efficient material allocation, which leads to more uniform stress distributions. At the same time, for complex phenomena such as buckling, geometric or topological features (e.g., length of a single beam or local connectivity) at the unit cell level could entirely govern the global mechanical response of a lattice either triggering local instability or due to periodicity generating long-wave buckling phenomena (namely, global buckling)¹⁹. Although controlling local features of periodic lattice designs would in principle allow for fully tuning the mechanical response, rather simple unit cell designs, such as diagonally reinforced square grids, are usually employed in modern structural applications. Here, we inverse design periodic truss lattices for complex phenomena (such as structural instability) by non-uniformly assembling smaller building blocks, thus exploiting periodicity and local features control in order to obtain mechanically efficient yet fully controllable lattices. Guided by machine learning (ML) in a bottom-up fashion, small different building blocks (Fig. 1b) are connected together to shape a more complex unit cell (Fig. 1d), which in turn is tessellated to build a periodic architecture (Fig. 1g).

With the recent advances in ML and additive manufacturing, tailoring the structure of lattice materials for a targeted property, namely inverse design, has become progressively more feasible, mainly thanks to the possibility of efficiently exploring larger

design spaces and manufacturing complex geometries. From the computational side, deep-learning models²⁰, specifically, represent a promising alternative to physics-based models for materials design, providing much faster (several orders of magnitude) yet accurate structure-property relationship predictions, thus allowing efficient design space exploration^{21–28}. From composites^{29–33}, through complex symmetric architected materials³⁴, stretchable kirigami-inspired-cut materials^{35,36}, spinoid metamaterials³⁷, up to polycrystalline solids³⁸, several studies have attempted to solve the inverse design problem exploiting the powerful computational and predictive capabilities provided by deep-learning techniques, mainly deep neural networks, used either as generative^{31,36,39,40} or surrogate forward models coupled with other optimization methods^{32,41} (e.g., evolutionary algorithms). Yet, only a few studies have provided solutions for the inverse design of truss lattice materials, mainly focusing on (i) pre-existing architectures conveniently modified to obtain lattices with desired properties, such as tunable stiffness anisotropy⁴² and stronger micro-lattices with arranged defects⁴³; (ii) single complex 3D novel unit cells with load carrying applications, such as stronger lattice cores for sandwich structures^{44,45}; (iii) basic architectures (such as a square lattice), on which reinforcements are non-uniformly added in order to match the desired mechanical response from a database⁴⁶; (iv) targeted linear properties (in solid mechanics terms), such as lattice' stiffness^{39,41,42,47} and Poisson's ratio⁴⁸. To solve the inverse-design problem of lattice materials, we propose a bottom-up approach using a fully connected deep neural network (DNN) (as a decider) in conjunction with a genetic algorithm (as a sampler) to search for optimal architecture candidates, whose engineering applications are later verified by finite element (FE) simulations and experiments on 3D-printed lattices. It is worth underlying that the idea of combining an ML model with a genetic algorithm to solve inverse problems is not new in general^{24,32,41,49}. In solid mechanics, specifically, strong yet tough polycrystalline materials subject to complex fracture mechanisms^{38,50} (e.g., crack branching) as well as stiff and strong digital composites³² have been inverse-designed by exploiting

¹Department of Mechanical and Industrial Engineering, Norwegian University of Science and Technology (NTNU), Trondheim 7491, Norway. ✉email: marco.maurizi@ntnu.no

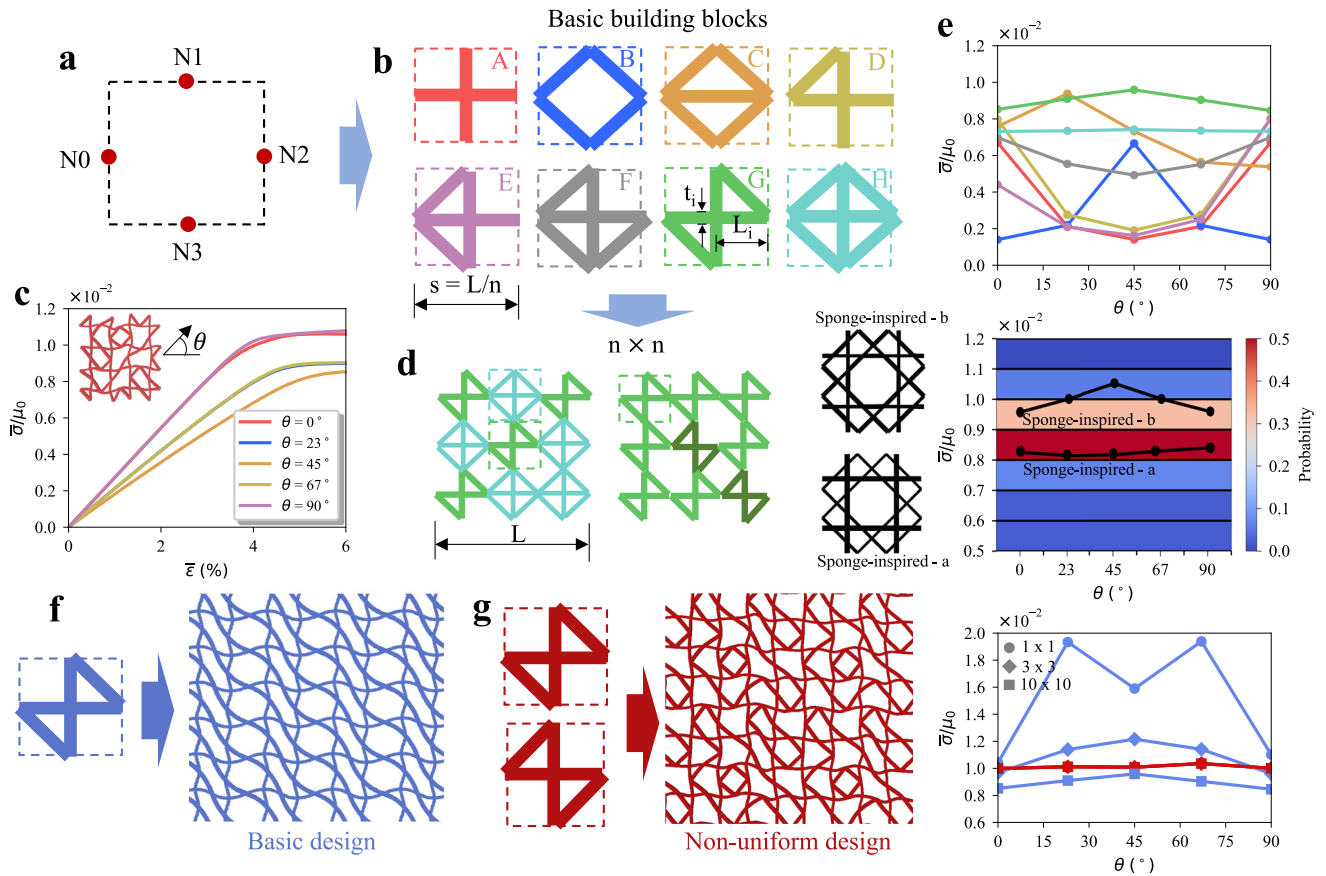


Fig. 1 Non-uniformly assembled lattices. **a** Initial squared framework with one node per edge (i.e., boundary nodes), identified by N0, N1, N2, N3 for building block generation. **b** Unique beam-based building blocks generated by combinatorially connecting the boundary nodes. **c** Typical stress–strain curves of non-uniform unit cells under uniaxial compression at five different loading directions ($\theta \in [0^\circ, 23^\circ, 45^\circ, 67^\circ, 90^\circ]$). Note that PBCs are imposed with a maximum applied effective strain of 6%. **d** Examples of $n \times n$ non-uniform unit cells with $n = 3$ composed of two different combinations of building blocks i.e., design G and H, and design G and its 90° -rotated version (identified by a darker green). **e** Upper panel: normalized effective buckling strength of the basic building blocks (in **b**) as a function of the loading angle θ . The superior quasi-isotropic buckling performance of design G are clear. Central panel: probability that a 4×4 non-uniform unit cell exhibits a normalized effective buckling strength within discretized levels (amplitude 0.1×10^{-2}). The data with $\Omega \geq 2\%$ are filtered out. Buckling values for sponge-inspired design are added as well as corresponding unit cells. Lower panel: effect of global buckling of uniform (in **f**) vs. non-uniform (in **g**) design on the buckling strength (colors refer to **f** and **g**). Lines are plotted only to facilitate the interpretation. **f** Post-buckled shape of a basic uniform design obtained tessellating a single building block (G in this case). Long-wave buckling instability is clearly exhibited. **g** Post-buckled shape of a non-uniform design obtained by combining two building blocks (G and its 90° -rotated version). *Sponge-inspired designs* (a: constant mass ratio of 0.5 between diagonal and non-diagonal beams; b: constant slenderness ratio). All values are obtained by FE simulations (see “Methods” section for details).

deep learning models as efficient surrogate solvers combined with genetic algorithms. We hence take advantage of the demonstrated ability of this combined model to discover high-performing designs in complex mechanics applications and simplicity, applying it in a bottom-up framework to inverse-design truss lattices undergoing high nonlinear phenomena (see next). Our simple yet effective approach aims first to overcome the previous issues: without relying on human intuition for choosing pre-existing structures as in (i), allowing the possibility to harness really simple building blocks instead of complex unit cells as in (ii) and to simultaneously exploit the advantages of periodicity and local features control without the need to simulate the whole design space as in (iii). The universal approximation capabilities of fully-connected DNN⁵¹ are fully exploited via Bayesian optimization of its architecture (see the “Materials and methods” section), using the DNN as a predictor of nonlinear buckling strength in the inverse design process, involving much more complex physical phenomena (geometrical and material nonlinearities; details next and in the “Materials and methods” section) than those determining the stiffness of lattices at small strains as in (iv).

Owing to the favorable vectorial (numerical) representation of the assembled unit cells together with the loading direction (numbers represent individual building block types and loading angle; see next for details) and its low training cost, a fully connected DNN is preferred over convolutional and graph DNNs. As a suggestion for future works, a compound of convolutional and fully-connected layers may be designed to deal with both the matrix data representing the unit cell and the scalar value representing the loading direction, possibly leading to higher accuracy; alternatively, harnessing the natural graph representation of lattice structures, graph DNNs may be employed, at the cost of more expensive training. However, it is not clear yet which network architectures guarantee higher prediction performance for truss lattice materials subject to complex phenomena. This work overall demonstrates that ML-based approaches can defeat human engineering intuition (historically, based on trial-and-error methods) and bio-inspiration in designing robust lattice architectures, comparing the discovered solutions to standard and bio-inspired grid-like designs. In addition, based on the ML-discovered solutions and their benchmark against bio-inspired designs, this

work attempts to provide insights into the mechanical stability of lattice materials, confirming also previously formulated hypotheses on the evolutionary advantage of the skeleton's architecture of deep-sea glass sponges¹⁷.

We propose a bottom-up deep-learning-based approach for the inverse design of non-uniformly assembled lattice materials, using the buckling strength as an example targeted property. This study is motivated by the impact that super-buckling-resistant architectures may have on practical engineering applications. Specifically, we aim at finding non-uniformly assembled 2D unit cell designs that maximize the effective buckling strength (i.e., homogenized value over the lattice); nevertheless, applications of our approach could be extended to 3D structures. Firstly, for simplicity we consider squared building blocks with one boundary node per edge (identified by N0, N1, N2, N3 in Fig. 1a), connected through beams; however, different boundary connectivity (e.g., two nodes per edge) could be arbitrarily adopted. To reduce the bias introduced by human decisions, our building blocks are formed by considering all the possible combinations obtained by connecting each boundary node to the other such that no nodes are left unconnected; eight building blocks are therefore obtained (indicated from A to H in Fig. 1b), without including reflection and rotation symmetries in the count (see Supplementary Fig. 1). It is worth noting that (1) one additional lattice node at the building block's center is created when the boundary node pairs N0–N2, N1–N3 are connected and (2) the boundary node connectivity changes between building blocks. From (1) follows that building blocks B and C have 4 nodes instead of 5 like the others, while (1) and (2) together lead to a different topology between building blocks. Our goal is thus to combine these building blocks to obtain buckling-resistant architectures. To pursue this objective, we first analyze the nonlinear post-buckling behavior of our building blocks under uniaxial compression by FE simulations (see the “Materials and methods” section for details). Since many applications require mechanical isotropy³⁴, quasi-isotropic architectures are preferred; thus, anisotropy is taken into account by evaluating the lattice's buckling response at five different loading directions (θ) 0°, 23°, 45°, 67°, 90°. To have a fair comparison between different designs, we assume a constant relative density, equivalent to that of the buckling super-resistant *Euplectella* glass sponge-inspired design suggested by M.C. Fernandes et al.¹⁷, which proved to outperform traditional square-based reinforced architectures. Motivated by the basic physics of buckling of a single beam, we also assume a constant slenderness ratio (next identified with k) for each beam of each building block. At a given relative density and topology, the slenderness ratio will be consequently deduced, leading to different values among the basic building blocks (see Supplementary Section 1). The performance of the different architectures is therefore evaluated by a fitness function $f = (\sum_{i=1}^5 \bar{\sigma}_{\theta_i} / \mu_0) (1 - \Omega)$, which takes into account the average effective buckling strength ($\bar{\sigma}_{\theta}$) along the different loading directions and the degree of isotropy $\Omega = \Delta \bar{\sigma}_{\theta} / \bar{\sigma}_{\theta, mean}$, where $\Delta \bar{\sigma}_{\theta} = (\bar{\sigma}_{\theta, max} - \bar{\sigma}_{\theta, min}) / 2$ and $\bar{\sigma}_{\theta, mean} = (\bar{\sigma}_{\theta, max} + \bar{\sigma}_{\theta, min}) / 2$, defined analogously as in ref.³⁴ but for buckling; μ_0 is the initial shear modulus of the incompressible hyperelastic (nonlinear) base material model adopted (see next, and “Materials and methods” section for details). The smaller the value of Ω , the more isotropic is the material in terms of buckling. Based on their fitness values (Fig. 1e and Supplementary Fig. 2b), the top-performing building block/s is/are then selected to be combined to form a $n \times n$ unit cell (Fig. 1d), which in turn can be tessellated to generate periodic patterns, as shown in Fig. 1f, g (or not if finite-size structures are needed). Encoding the $n \times n$ combination of building blocks into a numerical representation (for example, a binary representation of two building blocks is used), we then employ a DNN in conjunction with a genetic algorithm (GA) to find optimal combinations, based on the previous fitness function. The DNN is trained on a 4×4 dataset, composed by randomly picking geometries from the design space. In general, for a $n \times n$ unit cell and m building blocks, a total of m^{n^2} combinations exist, quickly

leading to astronomically large design spaces. For $m = 2, 16, 512$ and $65,536$ possible unit cells can be easily generated for the $2 \times 2, 3 \times 3$, and 4×4 design space, respectively. As suggested by C. Ma et al.⁴⁶, the horizontal and vertical reflection, and 180°- rotation symmetries are then excluded from the possible patterns to simulate, having identical mechanical response under uniaxial compression to their counterparts; nonetheless, they are included in the training dataset to inform the DNN, which could not otherwise distinguish symmetric transformations. Our design space comprises thus 16,576 unit cells with unique buckling responses. Figure 2 shows the inverse design optimization scheme. A classic genetic algorithm (GA) searches into the design space by cross-over and mutation, starting from a random population extracted from the 4×4 datasets, while the pre-trained DNN evaluates $\bar{\sigma}(\theta) / \mu_0$ for each individual of the population, by which the fitness function is then computed and used to discriminate the architectures' performance (next further details and in the “Materials and methods” section). Our optimal lattice architectures exhibit similar and even superior (depending on the loading direction) effective buckling strength compared to the recently suggested buckling super-resistant glass sponge-inspired design¹⁷ (reported for clarity in the central panel of Fig. 1e; details explained next and in Supplementary Section 2), providing also an opportunity to re-think the design of classic grid-like structures, based on engineering intuition. While these latter are rather geometrically simple (e.g., square lattice with cross reinforcements), the discovered designs exhibit quite complex resulting periodic patterns, demonstrating that standard structures are not optimal designs for buckling strength (see the section “Testing the high-performing lattices” and see the section “Discussion”). Finite-size versions of the optimal lattices are also fabricated by stereolithography and tested under uniaxial compression, confirming the super buckling resistance of the ML-discovered candidates (comparable to high-performing bio-inspired solutions) and the advantage of non-uniformly assembling unit cells.

RESULTS

Non-uniformly assembled architectures

Beam-based lattices are essentially ordered, often complex, arrangements of struts connected to each other at some locations, called nodes. Inverse designing them could be challenging if one wants to preserve their inherent graph structure, without using image-based representations^{34,39}, through which topological features, such as the number of nodes and connectivity (i.e., number of struts per node), cannot be explicitly controlled (implicitly, would be controllable, but with high computational costs). In dealing with the graph-based representation of lattices, we recognize two main inverse design approaches: top-down and bottom-up. In the first category, we classify those methods which mainly start from a basic periodic architecture and modify it to tune some mechanical properties, such as stiffness anisotropy⁴². Instead, we define bottom-up approaches those in which basic building blocks are employed to construct a more complex and performing architecture⁴³. If the local modifications of struts' shape and dimensions, and base material properties (typical of top-down approaches) allow for locally tuning the mechanical response of known lattices, on the other hand, the design space is limited by the adopted architecture's topology. Instead, bottom-up approaches allow wider control of geometry and topology, at the cost of increasing the complexity and dimension of the design space in which searching for optimal architectures.

In this work, we adopt a bottom-up inverse design approach that allows us to arbitrarily compose geometries, also with variable topology, with the only constraint of boundary nodes matching (see Fig. 1a, b). In this context, we prove how non-uniformly assembled architectures provide higher buckling strength and allow the destruction of global effects, such as long-wave buckling

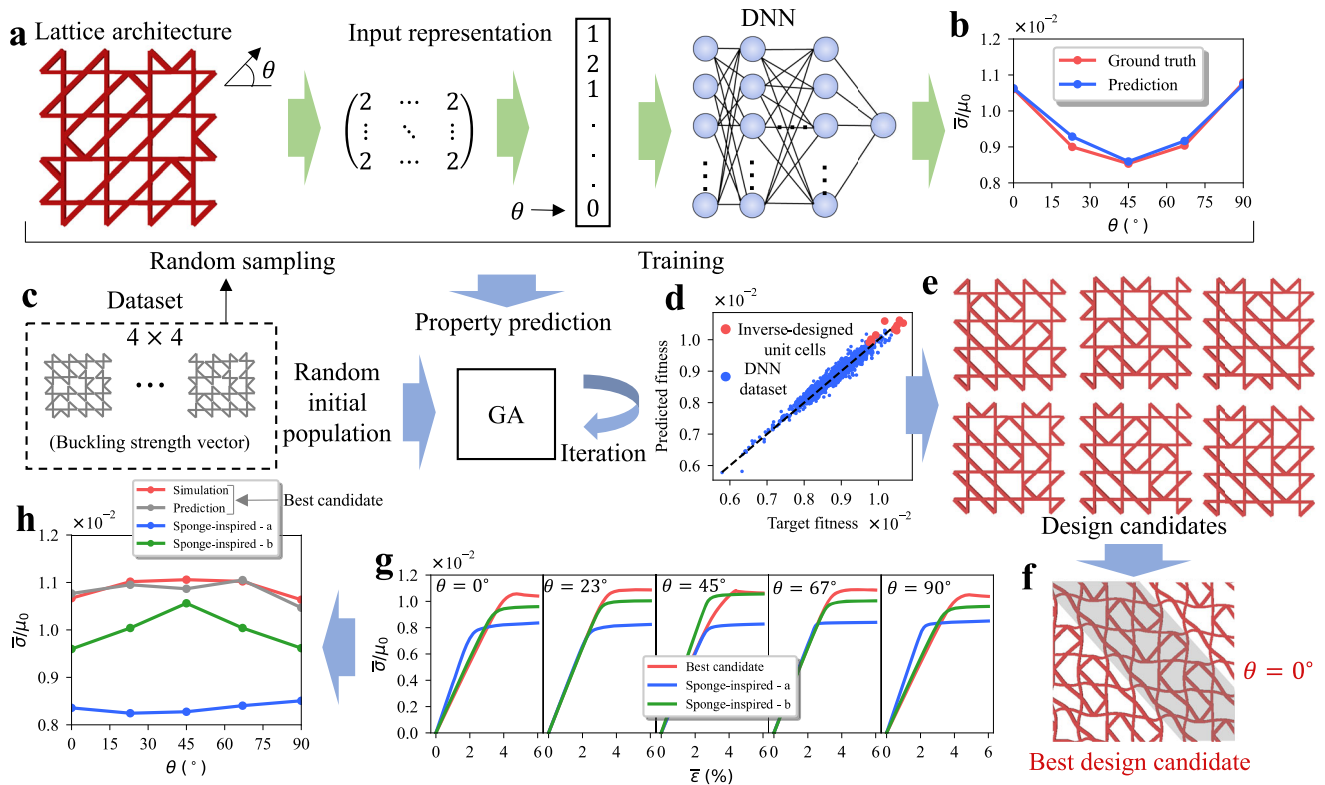


Fig. 2 Inverse design of buckling-resistant lattice materials. **a** Schematic information flow during property (buckling strength) prediction using DNN. **b** Example of predicted vs. target (ground truth) property of a generic non-uniform 4×4 unit cell. Lines are plotted only to facilitate the interpretation. **c** Dataset used for training and testing the DNN. **d** Predicted vs. target fitness values for the whole dataset and for 12 inverse-designed architectures. **e** Best 6 design candidates output by the inverse-design algorithm. **f** Simulated post-buckled shape of the first best design candidate loaded at $\theta = 0^\circ$. PBCs are imposed on a 10×10 super-cell. **g** Simulated stress-strain curves of the first design candidate and sponge-inspired designs at five different loading angles. **h** Normalized effective buckling strength of the first design candidate at different loading directions compared to that of the sponge-inspired designs. Lines are plotted only to facilitate the interpretation. To compare the DNN predictions with the FE-simulated values, in **g** and **h** a single unit cell with PBCs is considered; a slight decrease in performance is exhibited due to global buckling effects, as shown in Supplementary Fig. 8.

phenomena, which strongly reduce buckling resistance¹⁹. Figure 1f and g shows a comparison between the basic uniform design generated by tessellating a single building block (G in Fig. 1b) and a non-uniform design obtained by the composition of the same building block (G) with its 90° -rotated version (indicated as U in Supplementary Fig. 1). Comparing the two post-buckling deformed shapes suggests that the non-uniform design does not exhibit global buckling. This result is confirmed by comparing the effect of increasing the number of unit cells (obtaining a 'super-cell') for the basic and non-uniform design, as reported in the lower panel of Fig. 1e. It is worth underlying we adopt periodic boundary conditions (PBCs) (see the section "Materials and methods") to avoid boundary effects and speed up the simulations in view of using these latter as training and test data for the DNN. The periodicity assumption does not restrict the general validity of the proposed inverse-design approach: finite-size lattice structures could be also generated either assuming the dimension L in Fig. 1d to match that of the finite architecture or iteratively tessellating the space with two or more unit cells (created at the previous iteration), generating a new unit cell at a greater scale, and so on until the finite targeted size is reached.

Based on the physics of buckling of beams (Supplementary Section 1), we generate our architectures assuming a constant slenderness ratio for each beam of each building block, defined as $k = t_i/L_i$, where t_i and L_i are the thickness and node-to-node length of the single i th strut, respectively (see Fig. 1b, and Supplementary Section 1 for detailed values). This assumption represents the only yet important physics knowledge we input into the inverse-design

algorithm. It is worth indeed observing that building block G can alone reach high buckling strength and fitness values (Supplementary Fig. 2b), compared to classic (building blocks A and C) and bio-inspired designs, as shown in the upper and middle panels of Fig. 1e. Comparing design G with the other building blocks' buckling behavior thus suggests that a combined effect between topology and number of beams exists. We postulate that under the assumption of constant volume fraction and slenderness ratio there should be a threshold in the number of beams/connectivity over which the compressive buckling strength does not increase anymore, and tensile strength is promoted; being outside the scope of this work, we left further analyses for future research. While our targeted property for inverse design is the buckling strength, we report for completeness in Supplementary Fig. 2c the effective normalized stiffness of the single building blocks, which overall show slight anisotropic behavior as typical grid-like structures¹⁷. Note that design G exhibits similar average stiffness values compared to sponge-inspired designs (see Supplementary Figs. 2c and 7b; later explained in detail). Our inverse-design approach could in principle be extended to perform multi-objective optimizations (i.e., using two or more targeted properties), paving the way for future research directions.

The central panel in Fig. 1e shows the probability that a 4×4 non-uniform design (obtained by tessellating the building block G and its 90° -rotated version) exhibits a buckling strength in one of the highlighted ranges for each of the five considered loading directions. The diagram is constructed by selecting geometries from the 4×4 dataset (later used for DNN training and test) with a

degree of isotropy $\Omega < 2\%$ (quasi-isotropy). Unambiguously, most of the buckling quasi-isotropic geometries fall into the same range of the sponge-inspired designs; however, $\sim 40\%$ of the architectures in the selected dataset have higher buckling strength values than the sponge-inspired design-a (later explained in detail), up to a 30% increase. Important to underline that our designs have both a constant slenderness ratio (as sponge-inspired-b) and uniform material allocation between diagonal and non-diagonal beams (as sponge-inspired-a).

Nonlinear buckling resistance prediction

In this work, we employ an easily-to-train DNN (compared to generative neural networks^{34,36,39,52}) to predict the effective buckling strength of uniaxially compressed lattices. The trained DNN will then be used as a decider for the inverse design of non-uniformly assembled architectures. To avoid preferable collapsing loading directions in the inverse design algorithm, we let the DNN learn the relationship between lattice patterns and buckling strength at different loading angles ($\theta = 0^\circ, 23^\circ, 45^\circ, 67^\circ, 90^\circ$). From the performance of the single building blocks (upper panel Fig. 1e and Supplementary Fig. 2b) and their combinations (Supplementary Fig. 3), evaluated by the fitness function f (later employed in the inverse design algorithm), we select design G and its 90° -rotated version as optimum candidates for non-uniform assembly (more details in Supplementary Section 1). Specifically, we first simulate the nonlinear post-buckling behavior of the 4×4 non-uniform unit cells by (1) conducting an eigenvalue buckling analysis, (2) applying the lowest compressive eigenmode as a perturbation to the original structure, and (3) performing a nonlinear static analysis introducing large deformations and material nonlinearities (see the “Materials and methods” section for further details). To compare the performance of our optimal geometries with those of the incredibly robust sponge-inspired design, we adopt the analogous incompressible neo-Hookean material model as in ref. 17, describing a hyperelastic (nonlinear) behavior, with a shear modulus $\mu_0 = 14.5$ MPa. We identify the effective buckling strength from the corresponding stress-strain curves (see Fig. 1c) as the maximum stress reached before the final imposed strain of 6%, assuming only one buckling event occurs within this range of deformation. Using then the normalized value $\bar{\sigma}(\theta)/\mu_0$ as output and the mean squared error (MSE) as loss function, we train a DNN (details on the architecture in the “Materials and methods” section and Supplementary Section 3) on the previously simulated unit cells, which consist of 2000 geometries (i.e., $\sim 12\%$ of the total combinations) randomly extracted from the 4×4 design space (next, performance sensitivity on training data). Note that the horizontal and vertical reflections, and the 180° -rotations, having an identical mechanical response, are further included in the dataset, leading to a \sim three-fold data augmentation (i.e., increase of training data), helping to improve the prediction accuracy. As shown in Fig. 2a, to identify the input architectures with unique mechanical responses, the unit cells are firstly represented as matrices of integers, which identify the specific employed building blocks (i.e., 1 and 2 for two building blocks design); later, the matrices are vectorized to be input into the DNN. To further distinguish between different loading directions, the corresponding angle is thus concatenated to the vector representation. To find an optimal DNN architecture, we then perform a Bayesian optimization of the main network's hyperparameters i.e., number of layers, neurons in each layer, and learning rate (using the KerasTuner framework⁵³); for details on the optimization and optimal hyperparameters see the section “Materials and methods”.

A comparison between the DNN-predicted and numerical (i.e., ground truth) buckling strength of a randomly selected unit cell is shown in Fig. 2b. Although only five loading angles are considered (to limit the computational cost), the trend is essentially captured,

with a maximum 5% of mismatch on each direction for this particular case. To globally evaluate the regression performance of our DNN, we then employ a set of metrics, as in our previous work⁵⁴: the MSE, which is also the adopted loss function; the mean absolute error (MAE); the ratio between the MAE and the ground truth, namely the mean absolute percentage error (MAPE); the ratio between the MAE and the ground truth range, identified as RMAE; the coefficient of determination R^2 between the predicted values and the ground truth. A prediction accuracy is also used, defined as the fraction of values for which the RMAE $< c$, where c is an arbitrary threshold with values $0 < c < 1$; we assume here $c = 0.1$ is an acceptable value. In Fig. 3a–c we report some of these performance indicators only for the test data i.e., data never ‘seen’ by the DNN, while in Fig. 3d–f the corresponding metrics but for the average buckling strength values over the loading angles for all the simulated data, which will be called *average data*. Although providing a rough performance estimate for generic anisotropic behavior, average buckling values tend to be a good proxy for quasi-isotropic structures’ performance. Specifically, despite the difficult task of predicting instability in nonlinear post-buckling analyses, satisfactory predictions are obtained both for the test data and average data with $R^2 = 0.846 \pm 0.010$ and 0.952 ± 0.011 , respectively (one run shown in Fig. 3a and d). In addition, representing the absolute frequency in which each normalized buckling strength value occurs by a colored scale, independently of the loading angle, Fig. 3a confirms that most of the simulated data are well predicted by our DNN (being around the bisector line), and fall mainly around $0.85\text{--}0.9 \times 10^{-2}$ (confirming the central panel of Fig. 1e). The average data furthermore show better accuracy than the single angular values (see Supplementary Table 2), as expected from an ML regression algorithm.

In ML-based inverse design frameworks, the sensitivity of the predictor to the training density (i.e., a fraction of data used for training) is not negligible, especially for large design spaces. Here, to find an optimal amount of training data, we evaluate the DNN's performance change with training density ranging from 1% to 90%. The relative error distribution for the test and average data is reported in Fig. 3b and e, respectively. Increasing the training density, the variance of the distribution decreases, with the best performance around 80%, corresponding to ~ 1600 training architectures. These results are confirmed by the MAPE and prediction accuracy change, which display a similar convergence (Fig. 3c and f); we, therefore, set the optimal training density to $\sim 80\%$. Suitable performances are thus reached by our DNN, whose function together with GA is to find a set of high-performing candidates that are then validated by simulations and experiments. Supplementary Table 2 reports all the metrics measured for a training density of 80%. Despite the relatively small design space ($\sim 16,576$ unique architectures), we want to emphasize that highly nonlinear anisotropic post-buckling phenomena in lattice materials are captured by a rather simple DNN, which is able to predict the buckling strength at different loading directions.

Inverse design of buckling-resistant lattices

Combining DNN and GA, we provide a rather simple yet powerful property-oriented inverse design approach for truss lattice materials. Figure 2 shows a schematic of the design algorithm, while further details can be found in the section “Materials and methods” section. Briefly, the DNN is first trained and validated on the previously simulated datasets, corresponding to structure–property vector pairs (Fig. 2c). GA is then implemented to explore the design space, searching for optimal architectures i.e., ‘individuals’ (geometries) with higher fitness. It is worth noting that our fitness function takes into account the average buckling strength along different loading directions and the degree of buckling isotropy. Given the inherent random nature of the GA

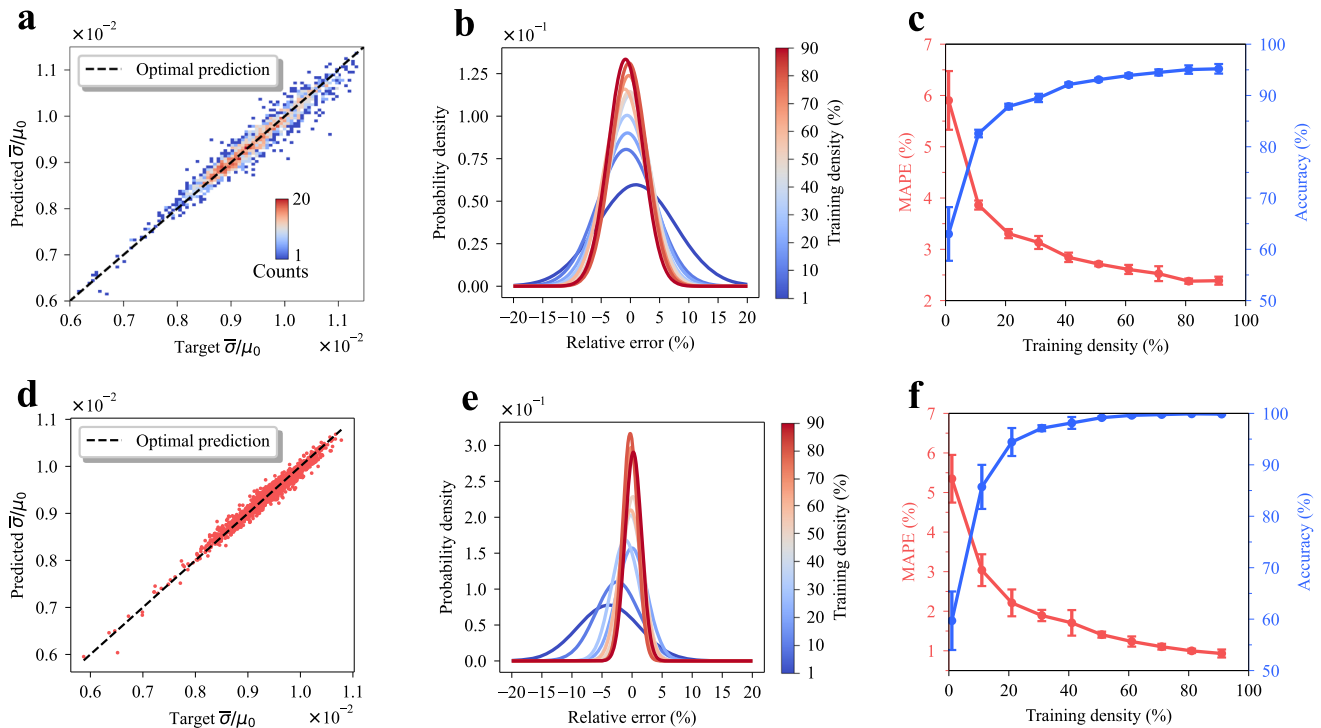


Fig. 3 Nonlinear buckling resistance prediction using DNN. **a** Predicted vs. target (simulated) normalized buckling strength values (on test data, never seen by the DNN). The number of times a value occurs is indicated as *Counts* (90 bins are selected in the 2D histogram). **b** Probability density of the percentage relative error between predicted and test data. A Gaussian density is assumed. **c** MAPE and accuracy values on test data plotted against training density. Lines are plotted only to facilitate the interpretation. **d** Predicted vs. target (simulated) normalized mean buckling strength values, averaged over the loading directions. **e** Probability density of the percentage relative error between predicted and average data. A Gaussian density is assumed. **f** MAPE and accuracy values on average data plotted against training density. One run, optimized network's hyperparameters and training density of 80% is considered, if not otherwise specified. Lines are plotted only to facilitate the interpretation. Error bars correspond to one standard deviation computed over 5 runs.

algorithm, we run optimization rounds for 100 iterations until 12 distinct design candidates are obtained, as shown in Fig. 2d. Based on the fitness value, a natural ranking is then deduced for the 12 candidates, and the best-performing 6 design candidates are selected (see Fig. 2e). Figure 2f reports the deformed buckled shape (for $\theta = 0^\circ$) of the best candidate (left-upper corner in Fig. 2e), highlighting the generated periodic pattern along the 45° -direction, which repeats itself alternately with a phase-delay. Hardly imaginable by humans, interesting high-performing patterns emerge by periodically tessellating the non-uniform designed unit cells. The periodic patterns of the best 6 design candidates are reported in Supplementary Fig. 6. We want to emphasize that the found architectures exhibit on an average better performance than those used for training and testing our DNN (Fig. 2d), suggesting that the proposed inverse design algorithm is able to discover new high-performing geometries.

To benchmark our results with other known architectures, we compare the best design candidate with the sponge-inspired design (control design), which has been found to exhibit an exceptional buckling strength, even greater than classic grid-like designs (square unit cells with 45° -reinforcements). To have a fair comparison, we consider two different versions of the sponge-inspired design (see Fig. 1e): (a) in which the volume ratio between diagonal and non-diagonal beams is constant and equal to 0.5; (b) in which the slenderness ratio is constant for each beam of the lattice; note that our inverse-designed architectures fulfill both constraints by construction. Figure 2g displays the effective stress-strain curves at five loading directions for the selected architecture and the sponge-inspired designs. While our geometry tends to buckle at larger effective stress values (except at $\theta = 45^\circ$), the control designs (a) and (b) exhibit similar or higher stiffness

(see Supplementary Fig. 7b). With thicker non-diagonal beams (along 0° and 90°), the sponge-inspired-a design, which resembles the real allocation of material in glass sponges, seems not to be globally optimized for buckling strength, but rather to fulfill a multiple-criteria optimization problem i.e., maximizing stiffness and buckling strength at the same time along the vertical and horizontal direction. On the contrary, as a result of a single-criterion optimization problem, the ML-designed unit cell exhibits higher buckling performance ($\sim 10\%$ than (b), and $\sim 30\%$ than (a)), demonstrating that target-specific ML-based solutions can out-perform bio-inspired solutions, which are usually not only subject to multiple structural but also biological constraints. These results hold also for different relative densities. Supplementary Fig. 9 reports the effect of relative density on the buckling performance of the three designs: using (a) as the control design and the fitness function as the performance indicator, the ML-designed architecture exhibits ~ 15 – 45% higher performance for relative densities in the range ~ 6 – 45% .

Relatively complex biological systems (such as deep-sea glass sponges) are subjected to biological and physiological constraints, such as growth, feeding, and locomotion, which may make some optimal structural solutions disadvantageous from a natural selection viewpoint or hard to obtain due to a different 'design space'. In the case of glass sponges, in the early stages of growth, to accommodate radial expansion the diagonal, horizontal, and vertical struts are not structurally joined together¹⁷. In addition, our hypothesis of constant slenderness ratio is unlikely to occur in glass sponges probably due to the advantage of having thicker horizontal and vertical struts, which provide higher stiffness along the tangential (corresponding to our $\theta = 0^\circ$) and longitudinal (corresponding to our $\theta = 90^\circ$) direction, respectively, as shown in Fig. 2g.

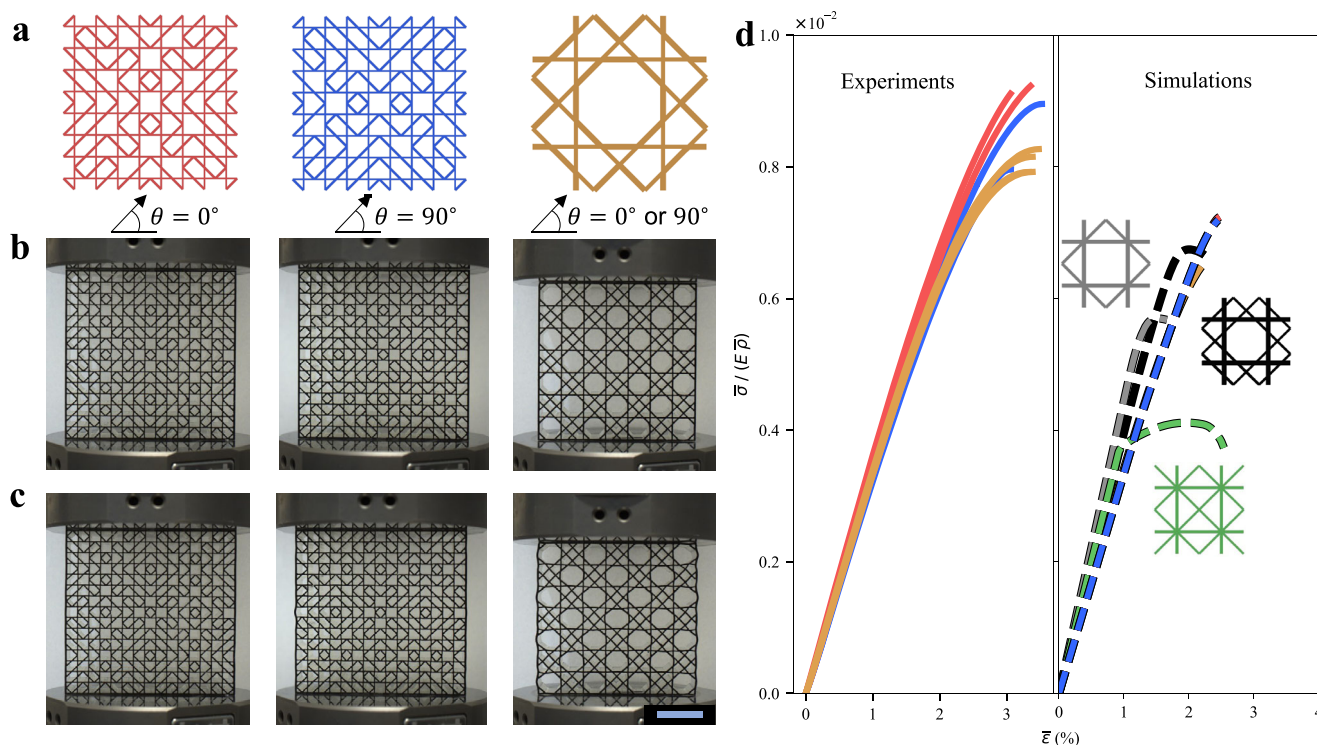


Fig. 4 Uniaxial compression experiments and simulations of 3D-printed finite-size lattices. **a** Experimentally tested unit cells. Snapshots of **b** un-deformed and **c** deformed (just before failure) 3D-printed samples at $\sim 3.3\%$ applied strain. **d** Normalized experimental and numerical stress-strain curves for the symmetric-inverse-designed architecture (at two different loading angles), sponge-inspired designs, and typical grid-like structures. The effective stress is normalized by the base material's Young's modulus (see the "Materials and methods" section) and relative density. $n = 4$ samples are tested for the symmetric-inverse-designed architecture (2 for each loading angle), while $n = 3$ samples for the sponge-inspired-b design. Curves are color-coded according to the unit cells depicted in (a) and (d). Scale bar 20 mm for (b) and (c).

These structural constraints are most likely responsible for the sponge' skeleton architecture. Nevertheless, a recent study⁵⁵ has provided evidence for the hydrodynamic function of the skeletal features of deep-sea glass sponges. It has demonstrated that the presence of fenestrae (apertures in the skeletal structure) tends to reduce the drag, which mitigates the stress experienced by the sponge and improves its mechanical stability⁵⁵. Structural and hydrodynamic advantages could thus jointly explain why the sponge's skeleton architecture largely differs from our optimal ML-derived buckling-resistant designs.

Testing the high-performing lattices

To significantly reduce the required computational time for training data generation, taking advantage of the assumed geometric periodicity of our lattices, the developed inverse-design algorithm relies on PBCs applied to individual unit cells (i.e., 1×1 super-cell), (see the "Materials and methods" section). However, for practical applications, finite-size structures have to be considered. To confirm the applicability of our inverse-design results, we thus fabricate (3D-printing stereolithography) and test (uniaxial compression) our ML-designed finite-size ($M \times M$ repeated unit cells) architectures and the sponge-inspired-b design as an optimal bio-inspired benchmark (see the section "Materials and methods" for details on manufacturing and testing). For further comparison, we simulate these architectures, the sponge-inspired-a, and other grid-like structures, namely, 45° -reinforced square and sponge-inspired lattice with a single diagonal beam (green and gray in Fig. 4d, respectively), with size and boundary conditions resembling those of the experimental tests (see the section "Materials and methods" section).

Motivated by asymmetric boundary effects (see Supplementary Fig. 13) in finite-size structures, we construct a crystallographic

pmm-symmetric (see ref. ³⁴ for details on 2D symmetry groups) version of our best design candidate by reflecting the single unit cell around the vertical and horizontal axis (Supplementary Fig. 14); experimental tests and simulations of the finite-size ML-designed structure are performed on this design.

To allow high-quality manufacturing (i.e., accordingly to the 3D-printer's resolution), we 3D print samples with nominal relative density $\bar{\rho} = 0.20$ (effect of relative density in Supplementary Section 6) and unit cell size $L = 20$ mm, except for the symmetric-inverse-designed architecture, whose cell measures $2L$ by construction. Based on these dimensions, to limit the maximum load reached during uniaxial compression below that of the machine's load cell, the structures comprise 2×2 and 4×4 tessellations of the symmetric-inverse-designed and sponge-inspired-b architecture, respectively (Fig. 4a). In addition, to demonstrate that the buckling performance gain of our architecture over other designs is likely independent of the material model, we use an elasto-plastic material (see the "Materials and methods" section) to fabricate the lattices (similar performance gain is numerically demonstrated by using the same hyperelastic material model adopted for the inverse-design, see Supplementary Fig. 24). We then compare the mechanical response of the considered structures under uniaxial compression along $\theta = 0^\circ$; however, to investigate possible asymmetries in the buckling response, our architecture is also tested and simulated along $\theta = 90^\circ$ (pmm-symmetry does not have 90° -rotation symmetry).

We first compare the experimental responses of the ML-designed and sponge-inspired-b structures (Fig. 4d). From the normalized stress-strain curves, $\sim 15\%$ overall average increase in load-carrying capacity is exhibited by the ML-designed architecture compared to the sponge-inspired design, confirming the previous results in Fig. 2g. It must be noted that our architecture

shows small deformations just before catastrophic failure compared to the sponge-inspired design, whose local deformation is more pronounced (see Fig. 4c and Supplementary Videos 1–2). In addition, the ML-designed structure seems to have higher effective stiffness and strength along the $\theta = 0^\circ$ loading direction compared to the $\theta = 90^\circ$ direction.

To validate these results as well as to compare the buckling performance of our design with other traditional grid-like structures, we then analyze the numerical stress-strain curves (for details on the material model, see the “Materials and methods” section and Supplementary Section 9). Contrary to what was expected based on the experimental results, the ML-designed structure is theoretically isotropic along the two loading directions. Because of the optimized buckling strength, our architecture is indeed less prone to buckle than the other designs, suggesting that it tends to fracture before buckling (as confirmed by the experiments in Fig. 4c). This result suggests that the larger difference between the stress-strain curves along $\theta = 0^\circ$ and $\theta = 90^\circ$ exhibited by the ML-designed tested samples can be considered as scatter due to the random nature of the brittle fracture. The 90° -symmetric buckling response of our design obtained by simulations is further confirmed by the similarity of the critical modes for $\theta = 0^\circ$ and 90° , as reported in Supplementary Figs. 17–20. The numerical results confirm first the experimental buckling performance gain of our design over the bio-inspired structures. Second, the ML-designed lattice exhibits ~30–90% higher maximum loading capacity compared to traditional grid-like designs (right plot in Fig. 4d), with a decrease in the effective stiffness. A trade-off between stiffness and strength hence appears evident, as found for the single unit cell subject to PBCs (see Fig. 2g). Future works may address the multi-objective optimization problem, where, for example, both stiffness and buckling strength is maximized. More analyses on the finite-size lattices can be found in Supplementary Section 10, such as the effect of buckling modes on the response (Supplementary Fig. 21), and the comparison between the experimental and numerical deformed shapes together with the local stress distribution at failure (Supplementary Fig. 22).

DISCUSSION

This work demonstrates in wider terms the powerful potentialities of a bottom-up ML-based approach to solve inverse design problems. More in detail, it mainly proves (1) the benefits of designing a more complex architecture by combining basic building blocks, whose performance can be individually easily evaluated; (2) the fruitful collaboration between DNN as decider and GA as a sampler to inverse design lattices; (3) the advantages of combining periodicity and local feature control in lattice materials. Selectively and quickly exploring the considered design space, our approach aims at dramatically speeding up the inverse design process, compared to traditional methods such as Edisonian trial and error (using simulations and experiments), bio-inspiration, and topology optimization (using simulations). Additionally, in the realm of beam-based lattice materials, topology undoubtedly plays an important role in determining mechanical properties. Despite the powerful capabilities shown by image-based ML inverse-design algorithms³⁴, they cannot explicitly control topological features of lattices, such as the number of nodes and connectivity. Our bottom-up ML-based approach attempts also to solve this problem, harnessing the possibility to control the topology of individual building blocks, with the constraint of matching boundary nodes (see Fig. 1a). Investigating the effects of non-uniform topology (as that obtainable by our approach) on the mechanical and fracture properties of lattices may represent one of the future challenges to address, with the goal to design and discover novel structurally performing materials.

With regard to buckling strength, some rather simple yet useful observations can be made by carefully analyzing the structure of building block G, which turned out to be (together with its 90° -rotated version) the most performing candidate for inverse designing optimal lattices. Its double 45° -reinforcement makes it on average (over the loading angles) stiffer (see Supplementary Fig. 2c) and stronger (see upper panel Fig. 1e and Supplementary Fig. 2b) than any other building block. Adding more diagonal reinforcements, such as in the blocks F and H (Fig. 1b), with the constraint of constant relative density and slenderness ratio, a decrease of beams' thickness is induced (leading on average to softer and weaker geometries); while, using fewer reinforcements as in the block D, the connectivity of the tessellated lattice is reduced (from 4 to 3, in this case), leading to weaker geometries. Another geometrical parameter, strictly related to the others, governing the buckling strength is the node-to-node length (i.e., L_i for the individual building block), which varies even if the topology of the tessellated lattice is unchanged. For example, the simple grid obtained by tessellating A has the same connectivity (i.e., 4) as that generated by tessellating G; however, the node-to-node length in the first lattice is twice that in the second one. This brings us to conclude that, under the assumption of constant relative density and slenderness ratio, the buckling strength of lattices is locally governed only by the interplay between connectivity, number of nodes, and node-to-node length. Global buckling additionally contributes to decreasing the buckling strength, emerging from the global tessellated pattern rather than the individual block's morphology.

By engineering intuition, traditional grid-like load-bearing structures are mainly designed starting from a square lattice, which guarantees easy construction and high vertical stiffness and adding cross reinforcements to avoid global instabilities due to vertical loads¹⁷. Bio-inspired designs, like glass sponge-inspired architecture, have demonstrated that engineering intuition is not actually effective in finding optimal lattice architectures, mainly due to the large design space offered by truss lattice materials. Based on this latter consideration, our ML-based approach attempts to go beyond human intuition and bio-inspiration. Comparing the traditional grid-like structures to the sponge-inspired design, an evident difference in the node-to-node lengths appears: the latter shows smaller lengths compared to the former (Fig. 4). As long as local buckling is the dominant instability mechanism, and the relative density and slenderness ratio are constant, the node-to-node lengths hence seem to govern the buckling strength of truss lattices, as intuitively expected based on the physics of buckling of simple beams (see Supplementary Section 1). However, our ML-designed architecture (Fig. 4a), although exhibiting similar or even higher buckling strength compared to the sponge-inspired design, is characterized by higher node-to-node lengths; this geometric feature can be captured by comparing an individual square cell of the ML-designed unit cell to that of the sponge-inspired one (comprising only one square) assuming they have the same size (Supplementary Fig. 23). This is somewhat surprising merely by physics intuition. It thus suggests that local buckling of lattices cannot be evaluated just by considering the individual lattice beams' instability; rather, the whole structure contributes to redistributing the deformation, leading to complex critical buckling shapes (Supplementary Figs. 17–20). Other existing optimization methods, such as topology optimization or image-based generative ML models, would not easily find such solutions due to their impossibility of (1) explicitly controlling the topology (e.g., number of nodes and connectivity) of the lattice, and (2) constraining the slenderness ratio of the individual beams to be throughout constant. Instead, our bottom-up approach allows us to decouple the topology from geometry: for example, varying the beams' geometry of each building block does not induce any change to the lattice connectivity. Based on (1) and (2), and on the strong

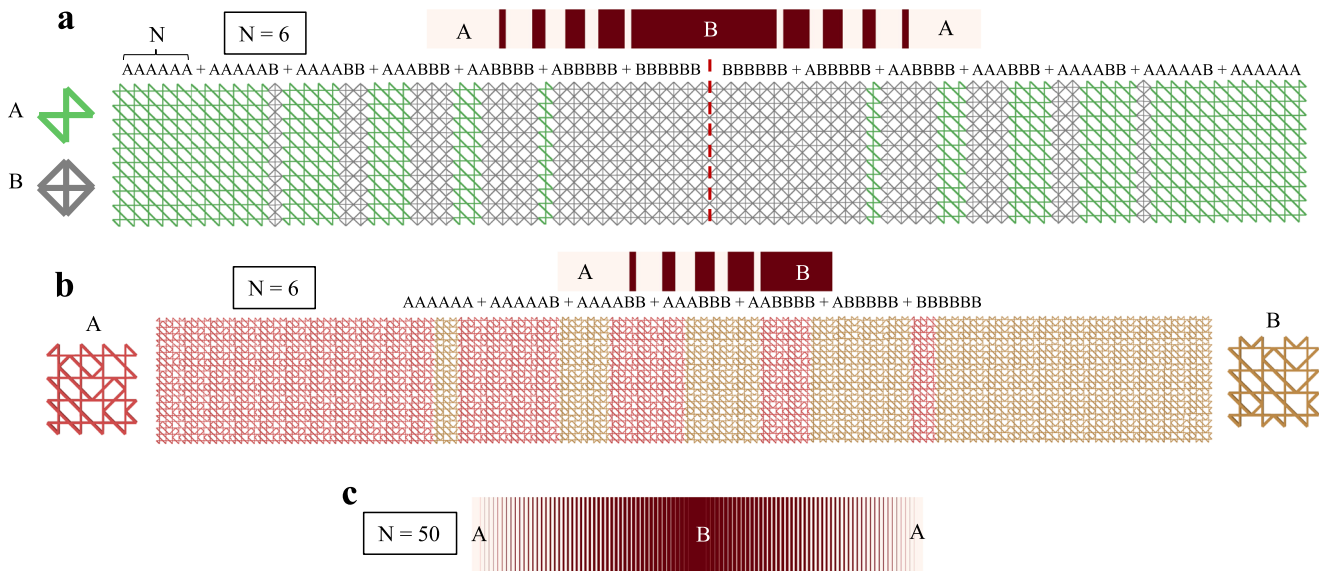


Fig. 5 Graded truss lattice materials using a building-block-based method. **a** Gradient of microstructures generated by symmetrically composing two elementary building blocks (from Fig. 1b) with $N = 6$ finite-length strings. The dashed red line represents the axis of symmetry. **b** Gradient of microstructures generated by composing two previously inverse-designed unit cells (from Fig. 2e) with $N = 6$ finite-length strings. A symmetric generation is not here shown for the sake of clarity in the visualization. **c** Example of gradient smoothness induced by increasing N to 50. A and B represent two different microstructures.

dependence of the topology-optimized solutions from the initial guess, we expect, even for relatively simple problems as the one treated here, the solutions proposed by our ML-guided approach to be hardly discoverable by classic optimization methods⁵⁶. To test the potential of alternative optimization algorithms, we also implement a Bayesian framework for inverse design, whose details and results are reported in Supplementary Section 7. Although a high-performing design is found, our discovered solution is not predicted by the implemented Bayesian algorithm. As a promising alternative inverse-design framework, an in-depth investigation of the surrogate model, search and acquisition function, required for the specific problem, is left for future research.

Functionally graded materials, often found in natural systems such as bone or bamboo, represent an example of non-uniformity, in which composition (e.g., volume fraction) and/or microstructure gradually change along some spatial directions. However, geometrical and topological non-uniformities have not yet been completely exploited for tuning the structural properties of man-made lattice materials. Our bottom-up ML-based approach could thus represent a starting point for future investigations of novel high-performing graded architected materials. Specifically, in Fig. 5 we show that our building-block-based method could be used to construct graded truss lattice materials by harnessing a string-based approach. By stacking finite-length (N) strings of letters (or numbers), representing combinations of individual building blocks, this method allows progressive changes in the architecture along one direction, generating a gradient of microstructures. Owing to the flexibility of the approach, either elementary building blocks (as in Fig. 1) or inverse-designed unit cells (as in Fig. 2) could be used as building blocks to shape materials with microstructure-driven graded properties (Fig. 5a and b, respectively), such as buckling resistance, stiffness or failure mechanisms. Graded architected materials could thus be hierarchically designed by our ML-guided algorithm: by composing distinct previously inverse-designed unit cells (Fig. 5b), an iterative application of the algorithm might much faster lead to optimal graded solutions compared to shaping the graded material starting from the elementary building blocks (of Fig. 1b). The flexibility of our building-block-based method though comes at a cost: smoother gradients (Fig. 5c) require higher computational

costs. To inverse-design high-performing materials, we believe future works will have to search for novel efficient ways to evaluate the performance of architected materials subject to complex nonlinear phenomena (such as buckling or path-dependent plasticity) at different length scales. Alternative solutions can be found in the natural truss lattice-to-graph mapping, by which graph neural networks might be exploited as a powerful predictive tool, taking into account topology changes, otherwise hardly controllable.

Harnessing our bottom-up ML-based inverse design approach, we have thus demonstrated that not only non-uniformly assembled lattices can exhibit high buckling resistance, even higher than bio-inspired and traditional architectures, opening an avenue for possible applications in modern structures and infrastructures, but also more complex architected materials could be generally designed with microstructure-driven graded properties.

MATERIALS AND METHODS

Finite element simulations

To create a dataset for training and testing our DNN and for validating the design candidates' output by our property-oriented inverse-design algorithm, FE simulations are performed using the commercial software Abaqus/Standard through Python scripting. All the models are meshed with 20 quadratic three-node 1-D Timoshenko-beam elements (identified as B22 in Abaqus) per strut, found to be an optimal mesh-insensitive value. Through the all-inverse-design process, an incompressible Neo-Hookean material model with initial shear modulus $\mu = 14.5$ MPa is adopted. Using this material model allows us first to validate our numerical results: resembling the simulations performed in ref. 17 on the sponge-inspired-a design indeed demonstrates that our simulations agree with the previous literature. Second, it provides a solid benchmark to compare our ML-designed lattices. Nonetheless, to prove that the hyperelastic model assumption does not limit the general validity of our approach, we also simulate unit cells (randomly extracted from the dataset) using a linear elastic material model (with equivalent Young's modulus $E = 2\mu_0(1 + \nu) = 43.5$ MPa, and Poisson's ratio $\nu = 0.5$, to the

hyperelastic model); the stress–strain curves of a randomly extracted geometry along the five loading directions ($\theta = [0^\circ, 23^\circ, 45^\circ, 67^\circ, 90^\circ]$) are reported in Supplementary Section 4. In addition, to reduce the computational cost, in an effort to find optimal periodic designs we impose periodic boundary conditions (PBCs) to each $n \times n$ unit cell. Note that outside the inverse design process for evaluating global buckling we also impose PBCs to $M \times M$ unit cells, where M is an integer value representing the number of times the single unit cell is repeated along the x - and y -direction. Occurring at larger length scales (i.e., long-wave phenomena), global buckling may not be captured by a single unit cell subject to PBCs. Therefore, analyzing the influence of M in $M \times M$ unit cells (forming a super-cell) subject to PBCs can help to identify possible long-wave phenomena. Roughly speaking, if the estimated buckling strength of a periodic lattice is reduced by increasing M , the lattice exhibits global buckling. Moreover, PBCs are also utilized when simulating individual building blocks. PBCs are applied to the unit cell's boundary through a set of virtual nodes, imposing the following 2D macroscopic deformation gradient:

$$\bar{F} = \begin{bmatrix} 1 - \sqrt{2E_{11} + 1} & 0 \\ 0 & \text{UNSET} \end{bmatrix} \quad (1)$$

corresponding to uniaxial compression conditions, in which E_{11} is the uniaxial component of the Green–Lagrangian strain tensor, used as a measure for finite strains. The first Piola–Kirchhoff stress tensor is then computed using the principle of virtual work⁵⁷, considering that it is work-conjugate to the deformation gradient \bar{F} . To evaluate the buckling strength at different loading directions, we rotate the model by an angle θ with respect to the uniaxial compression direction (i.e., x -direction), thus using the rotated coordinates for applying PBCs. For all buckling analyses, we first perform a linear eigenvalue buckling analysis and then perturbing the mesh of the model with the lowest compressive eigenmode, we conduct a nonlinear post-buckling analysis. For the linear analysis, five eigenvalues are computed and the lowest positive (i.e., which refers to compression instability in this case) value is adopted as the critical eigenvalue. To verify the applicability of the inverse-designed lattice, additional simulations of finite-size structures are also performed (checked against experimental results). To investigate the effect of a more complex material model in realistic finite-size structures, we adopt the material model calibrated to CLEAR resin (Formlabs). To capture the behavior of the uniaxially tested base material (Formlabs, CLEAR resin) up to failure, three material models are adopted: (1) linear elasticity with $E = 2200$ MPa and $\nu = 0.3$; (2) power-law hardening model $\sigma - S_y = H\epsilon^n$ to capture initial yield and hardening with $S_y = 28$ MPa, $H = 100$ MPa, $n = 0.25$; (3) linear damage evolution law defined by final fracture $\epsilon_f = 0.28$ (see Supplementary Section 9 for further details on the material model calibration). Depth for all the models is selected to avoid out-of-plane deformations, with a value of 20 mm. The effective stiffness of infinite lattices is computed by performing small-strain linear elastic analyses. Simulations are all performed on a 4-core Intel® Xeon® CPU E3-1270 V5 @3.60 GHz PC with 64 GB RAM.

DNN architecture

A classic fully connected deep neural network is adopted due to its powerful capabilities to approximate highly nonlinear relationships (i.e., effective buckling strength as a function of the architecture and loading direction), finding hidden patterns in data, to the possibility to deal with integer representation of inputs (i.e., representing the type of building block in this work), and to its simplicity for training. Hyperparameter tuning is first performed to find an optimal DNN's architecture, using Bayesian optimization in the KerasTuner framework⁵³; the training density is

kept constant and equal to 90% during the whole process. The base skeleton of the DNN's structure consists of an input layer that receives the vectorial representation of the lattice designs and the loading direction, appositely normalized to have zero mean and unitary variance, L successive layers each with n_i ($i = 1, \dots, L$) neurons and ReLU nonlinear activation function, and a single-output linear layer for regression; the first layer is associated with batch normalization to stabilize the learning process. During the hyperparameter optimization we let L and n_i vary between 2 and 6, and 32 and 288 with a step of 32, respectively. At the same time, the learning rate is also tuned between three values: 0.01, 0.005, and 0.001. The objective function for the Bayesian optimization is the validation loss function (i.e., the MSE), with a maximum number of trials (i.e., tested model configurations) of 20, each run for 100 epochs, with a batch of 64 samples, and a validation split corresponding to 10% of the training data. The resulting best parameters are $L = 6$, $n_1 = n_2 = n_4 = 288$, $n_3 = 32$, $n_5 = 192$ and $n_6 = 160$, learning rate of 0.005. Note that the output (i.e., $\bar{\sigma}(\theta)/\mu_0$) of the network is normalized into the range [0,1], and then re-scaled to obtain the original values during prediction. For the training density sensitivity, the best DNN architecture is trained to limit the number of epochs to 150 while using the early stopping technique to interrupt training after 30 epochs of no further validation loss reduction. For each training density value, 5 runs (including training and testing the network) are performed, randomly shuffling the data and utilizing the same batch size and validation split as before for each run.

Inverse-design algorithm

Searching for design candidates with high buckling strength, our inverse-design algorithm consists of a property predictor, identified by the DNN, and an explorer, identified by a GA. The pre-trained DNN serves as a surrogate solver to predict $\bar{\sigma}(\theta)/\mu_0$ at each iteration of the GA algorithm, which generates new designs based on the task-specific fitness function, which takes into account the effective normalized buckling strength ($\bar{\sigma}(\theta)/\mu_0$) and the degree of isotropy (Ω). GA is an evolutionary optimization algorithm that can be summarized into the following steps:

1. A random initial population (consisting of randomly picked designs from the database) is defined. Here it is set to be 2000.
2. The fitness function value is computed based on the DNN-predicted property value.
3. The individuals (designs) with the highest fitness are selected as parents for mating, producing the next generation of individuals (offspring). Here the number of parents is set to be 100.
4. Crossover is used to generate offspring. Here a center one-point crossover is adopted, leading to offspring with half of the genetic code of the first and second parent.
5. Mutation is then applied to the new offspring, allowing to change of the type of building block in each position of the unit cell (choosing between those used to build the database) with a low arbitrary probability. Here the mutation probability is set to be 0.01.
6. The new offspring with their parents form the new population.
7. The process is repeated for a prefixed number of generations, which here is set to be 100.

The algorithm is run until 12 unique designs are output. A further selection is made by selecting the best six architectures (highest fitness) of which FE simulations are performed to confirm the DNN predictions on the single unit cell. The highest-performing unit cell is then more deeply studied by FE simulations and experiments on 3D-printed finite-size structures.

Samples fabrication and testing

Finite-size structures are manufactured by stereolithography (SLA) using a 3D-printer Form 3 (Formlabs Inc., USA). The samples are 3D-printed along the out-of-plane lattice direction (namely, depth) with a layer thickness of 100 μm . After printing, the samples are cured with UV light (405 nm) at 60° for 60 min. To balance the trade-off between the 3D printer's resolution (25 μm on the plane) and the testing machine's maximum load, the lattices are fabricated with nominal relative density $\bar{\rho} = 0.20$ and unit cell size $L = 20$ mm. Quasi-static (strain rate of 0.001 s^{-1}) uniaxial compression tests are performed under displacement-control loading conditions on an Instron ElectroPuls1000 (Instron Inc., USA) with a 10 kN load cell. Details on the 3D-printed finite structures' dimensions can be found in Supplementary Section 10.

DATA AVAILABILITY

The data supporting the findings of this study are available within this article and its Supplementary Information. Additional data that support the findings of this study are available from the corresponding author on reasonable request.

CODE AVAILABILITY

The codes developed in this study are available from the authors upon reasonable request.

Received: 26 April 2022; Accepted: 14 November 2022;

Published online: 29 November 2022

REFERENCES

- Lakes, R. Materials with structural hierarchy. *Nature* **361**, 511–515 (1993).
- Wegst, U. G., Bai, H., Saiz, E., Tomsia, A. P. & Ritchie, R. O. Bioinspired structural materials. *Nat. Mater.* **14**, 23–36 (2015).
- Ortiz, C. & Boyce, M. C. Bioinspired structural materials. *Science* **319**, 1053–1054 (2008).
- Deshpande, V. S., Fleck, N. A. & Ashby, M. F. Effective properties of the octet-truss lattice material. *J. Mech. Phys. Solids* **49**, 1747–1769 (2001).
- Ashby, M. F. The properties of foams and lattices. *Philos. Trans. R. Soc. A* **364**, 15–30 (2006).
- Fleck, N. A., Deshpande, V. S. & Ashby, M. F. Micro-architected materials: past, present and future. *Proc. Math. Phys. Eng. Sci.* **466**, 2495–2516 (2010).
- Khaderi, S., Deshpande, V. & Fleck, N. The stiffness and strength of the gyroid lattice. *Int. J. Solids Struct.* **51**, 3866–3877 (2014).
- Hawreliak, J. A. et al. Dynamic behavior of engineered lattice materials. *Sci. Rep.* **6**, 1–7 (2016).
- Meza, L. R., Das, S. & Greer, J. R. Strong, lightweight, and recoverable three-dimensional ceramic nanolattices. *Science* **345**, 1322–1326 (2014).
- Meza, L. R. et al. Resilient 3d hierarchical architected metamaterials. *Proc. Natl Acad. Sci. USA* **112**, 11502–11507 (2015).
- Zhang, X., Vyatskikh, A., Gao, H., Greer, J. R. & Li, X. Lightweight, flaw-tolerant, and ultrastrong nanoarchitected carbon. *Proc. Natl Acad. Sci. USA* **116**, 6665–6672 (2019).
- Portela, C. M. et al. Supersonic impact resilience of nanoarchitected carbon. *Nat. Mater.* **20**, 1491–1497 (2021).
- Ye, J. et al. Ultra-low-density digitally architected carbon with a strutted tube-in-tube structure. *Nat. Mater.* **20**, 1498–1505 (2021).
- Wegst, U. & Ashby, M. The mechanical efficiency of natural materials. *Philos. Mag.* **84**, 2167–2186 (2004).
- Fratzl, P. & Weinkamer, R. Nature's hierarchical materials. *Prog. Mater. Sci.* **52**, 1263–1334 (2007).
- Aizenberg, J. et al. Skeleton of *Euplectella* sp.: structural hierarchy from the nanoscale to the macroscale. *Science* **309**, 275–278 (2005).
- Fernandes, M. C., Aizenberg, J., Weaver, J. C. & Bertoldi, K. Mechanically robust lattices inspired by deep-sea glass sponges. *Nat. Mater.* **20**, 237–241 (2021).
- Schaedler, T. A. et al. Ultralight metallic microlattices. *Science* **334**, 962–965 (2011).
- He, Y., Zhou, Y., Liu, Z. & Liew, K. Buckling and pattern transformation of modified periodic lattice structures. *Extrem. Mech. Lett.* **22**, 112–121 (2018).
- LeCun, Y., Bengio, Y. & Hinton, G. Deep learning. *Nature* **521**, 436–444 (2015).
- Pilania, G., Wang, C., Jiang, X., Rajasekaran, S. & Ramprasad, R. Accelerating materials property predictions using machine learning. *Sci. Rep.* **3**, 1–6 (2013).
- Lavecchia, A. Machine-learning approaches in drug discovery: methods and applications. *Drug Discov. Today* **20**, 318–331 (2015).
- Ramprasad, R., Batra, R., Pilania, G., Mannodi-Kanakkithodi, A. & Kim, C. Machine learning in materials informatics: recent applications and prospects. *NPJ Comput. Mater.* **3**, 1–13 (2017).
- Jennings, P. C., Lysgaard, S., Hummelshøj, J. S., Vegge, T. & Bligaard, T. Genetic algorithms for computational materials discovery accelerated by machine learning. *npj Comput. Mater.* **5**, 1–6 (2019).
- Hu, Y.-J. et al. Predicting densities and elastic moduli of sio2-based glasses by machine learning. *npj Comput. Mater.* **6**, 1–13 (2020).
- Kim, B., Lee, S. & Kim, J. Inverse design of porous materials using artificial neural networks. *Sci. Adv.* **6**, eaax9324 (2020).
- Tao, Q., Xu, P., Li, M. & Lu, W. Machine learning for perovskite materials design and discovery. *npj Comput. Mater.* **7**, 1–18 (2021).
- Zhang, J. et al. Design high-entropy carbide ceramics from machine learning. *npj Comput. Mater.* **8**, 1–12 (2022).
- Gu, G. X., Chen, C.-T. & Buehler, M. J. De novo composite design based on machine learning algorithm. *Extrem. Mech. Lett.* **18**, 19–28 (2018).
- Gu, G. X., Chen, C.-T., Richmond, D. J. & Buehler, M. J. Bioinspired hierarchical composite design using machine learning: simulation, additive manufacturing, and experiment. *Mater. Horiz.* **5**, 939–945 (2018).
- Chen, C.-T. & Gu, G. X. Generative deep neural networks for inverse materials design using backpropagation and active learning. *Adv. Sci.* **7**, 1902607 (2020).
- Kim, Y. et al. Deep learning framework for material design space exploration using active transfer learning and data augmentation. *npj Comput. Mater.* **7**, 1–7 (2021).
- Guo, K., Yang, Z., Yu, C.-H. & Buehler, M. J. Artificial intelligence and machine learning in design of mechanical materials. *Mater. Horiz.* **8**, 1153–1172 (2021).
- Mao, Y., He, Q. & Zhao, X. Designing complex architected materials with generative adversarial networks. *Sci. Adv.* **6**, eaaz4169 (2020).
- Hanakata, P. Z., Cubuk, E. D., Campbell, D. K. & Park, H. S. Accelerated search and design of stretchable graphene kirigami using machine learning. *Phys. Rev. Lett.* **121**, 255304 (2018).
- Hanakata, P. Z., Cubuk, E. D., Campbell, D. K. & Park, H. S. Forward and inverse design of kirigami via supervised autoencoder. *Phys. Rev. Res.* **2**, 042006 (2020).
- Kumar, S., Tan, S., Zheng, L. & Kochmann, D. M. Inverse-designed spinoid metamaterials. *npj Comput. Mater.* **6**, 1–10 (2020).
- Hsu, Y.-C., Yu, C.-H. & Buehler, M. J. Tuning mechanical properties in polycrystalline solids using a deep generative framework. *Adv. Eng. Mater.* **23**, 2001339 (2021).
- Wang, L. et al. Deep generative modeling for mechanistic-based learning and design of metamaterial systems. *Comput. Methods Appl. Mech. Eng.* **372**, 113377 (2020).
- Tan, R. K., Zhang, N. L. & Ye, W. A deep learning-based method for the design of microstructural materials. *Struct. Multidiscipl. Optim.* **61**, 1417–1438 (2020).
- Lee, S., Zhang, Z. & Gu, G. X. Generative machine learning algorithm for lattice structures with superior mechanical properties. *Mater. Horiz.* **9**, 952–960 (2022).
- Kulagin, R., Beygelzimer, Y., Estrin, Y., Schumilin, A. & Gumbsch, P. Architected lattice materials with tunable anisotropy: design and analysis of the material property space with the aid of machine learning. *Adv. Eng. Mater.* **22**, 2001069 (2020).
- Vangelatos, Z. et al. Strength through defects: a novel bayesian approach for the optimization of architected materials. *Sci. Adv.* **7**, eabk2218 (2021).
- Challapalli, A. & Li, G. Machine learning assisted design of new lattice core for sandwich structures with superior load carrying capacity. *Sci. Rep.* **11**, 1–10 (2021).
- Challapalli, A., Patel, D. & Li, G. Inverse machine learning framework for optimizing lightweight metamaterials. *Mater. Des.* **208**, 109937 (2021).
- Ma, C. et al. Accelerated design and characterization of non-uniform cellular materials via a machine-learning based framework. *npj Comput. Mater.* **6**, 1–8 (2020).
- Bastek, J.-H., Kumar, S., Telgen, B., Glaesener, R. N. & Kochmann, D. M. Inverting the structure–property map of truss metamaterials by deep learning. *Proc. Natl Acad. Sci. USA* **119**, 1 (2022).
- Kollmann, H. T., Abueidda, D. W., Koric, S., Guleryuz, E. & Sobh, N. A. Deep learning for topology optimization of 2d metamaterials. *Mater. Des.* **196**, 109098 (2020).
- Jiang, J., Chen, M. & Fan, J. A. Deep neural networks for the evaluation and design of photonic devices. *Nat. Rev. Mater.* **6**, 679–700 (2021).
- Lew, A. J. & Buehler, M. J. A deep learning augmented genetic algorithm approach to polycrystalline 2d material fracture discovery and design. *Appl. Phys. Rev.* **8**, 041414 (2021).
- Hornik, K. Approximation capabilities of multilayer feedforward networks. *Neural Netw.* **4**, 251–257 (1991).

52. Zheng, X., Chen, T.-T., Guo, X., Samitsu, S. & Watanabe, I. Controllable inverse design of auxetic metamaterials using deep learning. *Mater. Des.* **211**, 110178 (2021).
53. O'Malley, T. et al. Kerastuner. <https://github.com/keras-team/keras-tuner> (2019).
54. Maurizi, M., Gao, C. & Berto, F. Interlocking mechanism design based on deep-learning methods. *Appl. Eng. Sci.* **7**, 100056 (2021).
55. Falcucci, G. et al. Extreme flow simulations reveal skeletal adaptations of deep-sea sponges. *Nature* **595**, 537–541 (2021).
56. Ferrari, F. & Sigmund, O. Revisiting topology optimization with buckling constraints. *Struct. Multidiscipl. Optim.* **59**, 1401–1415 (2019).
57. Danielsson, M., Parks, D. & Boyce, M. Three-dimensional micromechanical modeling of voided polymeric materials. *J. Mech. Phys. Solids* **50**, 351–379 (2002).

AUTHOR CONTRIBUTIONS

M.M. conceived the idea, implemented the inverse-design algorithm, performed simulations and mechanical testing, and wrote the manuscript. M.M. and C.G. analyzed and discussed the results. C.G. and F.B. supervised the work. All authors reviewed the manuscript.

FUNDING

Open access funding provided by Norwegian University of Science and Technology.

COMPETING INTERESTS

The authors declare no competing interests.

ADDITIONAL INFORMATION

Supplementary information The online version contains supplementary material available at <https://doi.org/10.1038/s41524-022-00938-w>.

Correspondence and requests for materials should be addressed to Marco Maurizi.

Reprints and permission information is available at <http://www.nature.com/reprints>

Publisher's note Springer Nature remains neutral with regard to jurisdictional claims in published maps and institutional affiliations.



Open Access This article is licensed under a Creative Commons Attribution 4.0 International License, which permits use, sharing, adaptation, distribution and reproduction in any medium or format, as long as you give appropriate credit to the original author(s) and the source, provide a link to the Creative Commons license, and indicate if changes were made. The images or other third party material in this article are included in the article's Creative Commons license, unless indicated otherwise in a credit line to the material. If material is not included in the article's Creative Commons license and your intended use is not permitted by statutory regulation or exceeds the permitted use, you will need to obtain permission directly from the copyright holder. To view a copy of this license, visit <http://creativecommons.org/licenses/by/4.0/>.

© The Author(s) 2022